Electronic Supplementary Material (ESI) for Nanoscale.

Supplementary Information

Helically Aligned Fused Carbon Hollow Nanospheres with Chiral Discrimination Ability

Jun Maruyama,* Shohei Maruyama, Yukiyasu Kashiwagi, Mitsuru Watanabe, Tsutomu Shinagawa, Toru Nagaoka, Toshiyuki Tamai, Naoya Ryu, Koichi Matsuo, Mao Ohwada, Koki Chida, Takeharu Yoshii, Hirotomo Nishihara, Fumito Tani, and Hiroshi Uyama

Chiral Space in Helically Aligned Fused CHNSs on MWCNTs

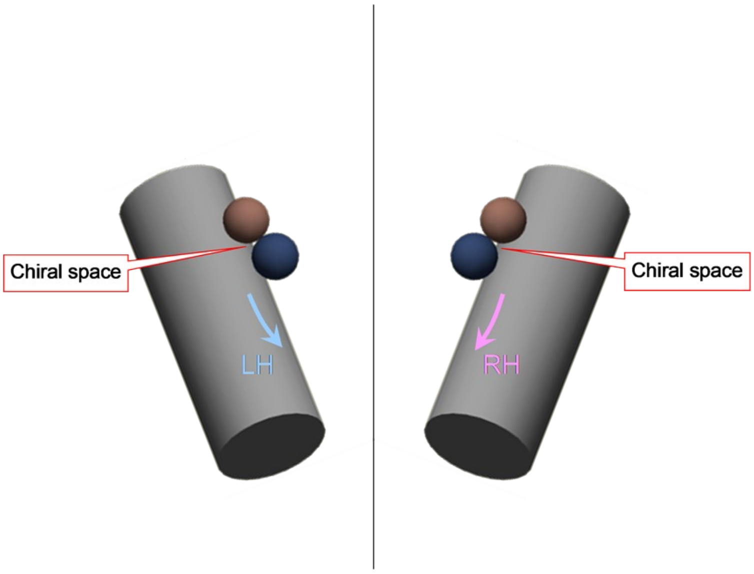

Figure S1. Schematic of the chiral space generated between MWCNTs and the outer surfaces of CHNSs aligned in the right-handed (RH) and left-handed (LH) helices. Two adjacent CHNSs and an MWCNT (the cylinder) are shown in different colors for simplification. An interactive PDF file containing a 3D model of the LH alignment is provided as other supplementary information.

Inhomogeneous Composite Formed Using Dispersed MWCNTs

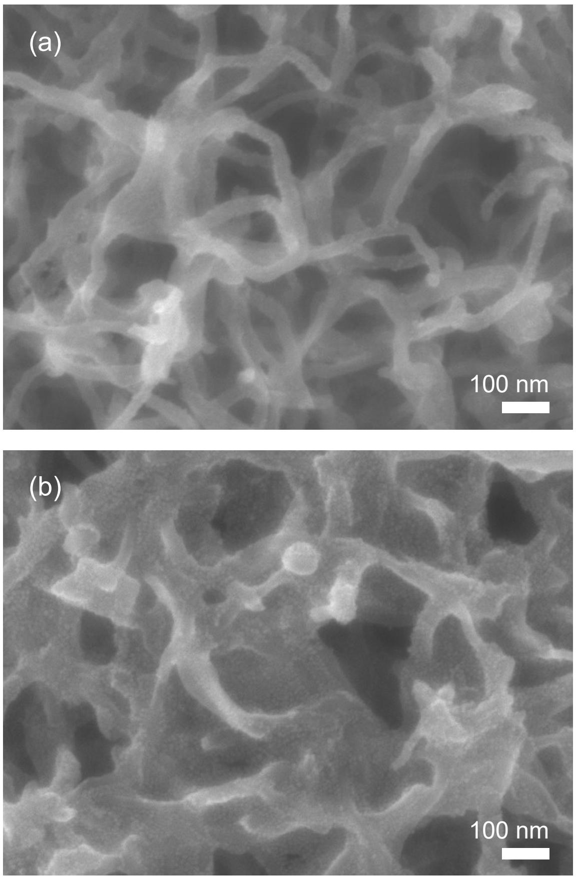

Figure S2. FESEM images of the top (a) and bottom (b) surfaces of a composite prepared by slow solvent evaporation from a mixture of ultrasonically dispersed MWCNTs, Fe_3O_4 NP dispersion, EC, and chiral inducer in a crucible, followed by carbonization at 550 °C. A minimal amount of Fe_3O_4 was loaded on the MWCNTs at the top surface, whereas an excessive amount was loaded at the bottom.

Magnified FESEM Images of C-EC-NP-S and C-EC-NP-R

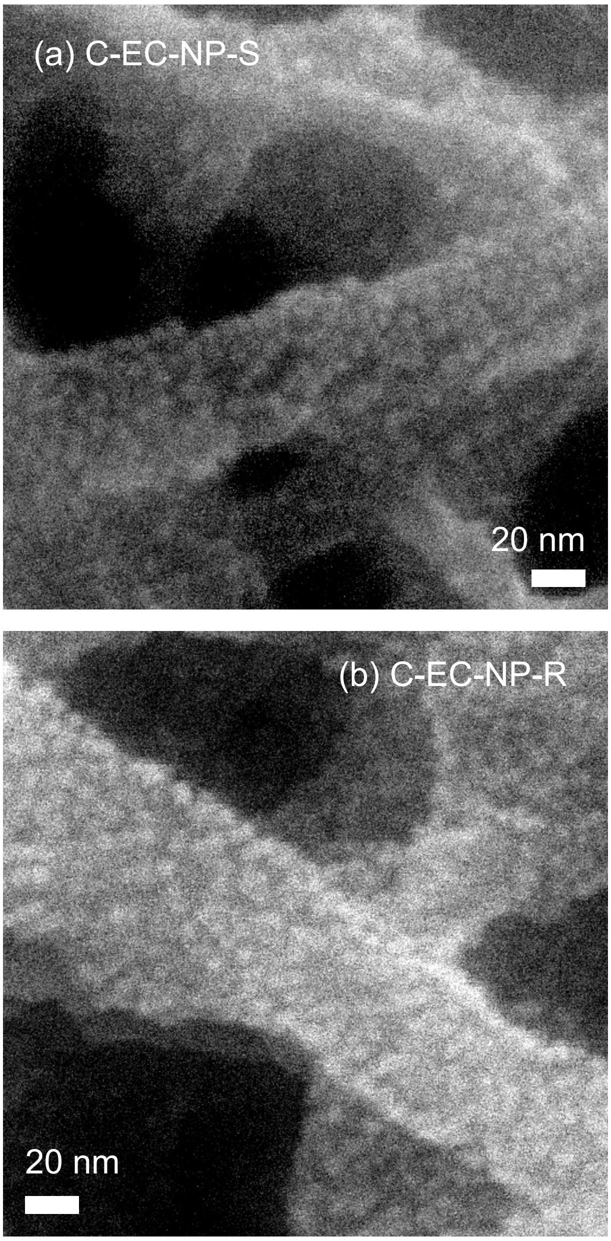

Figure S3. Magnified FESEM images of C-EC-NP-S (a) and C-EC-NP-R (b).

Reproducibility of VUVCD spectra and reference spectrum

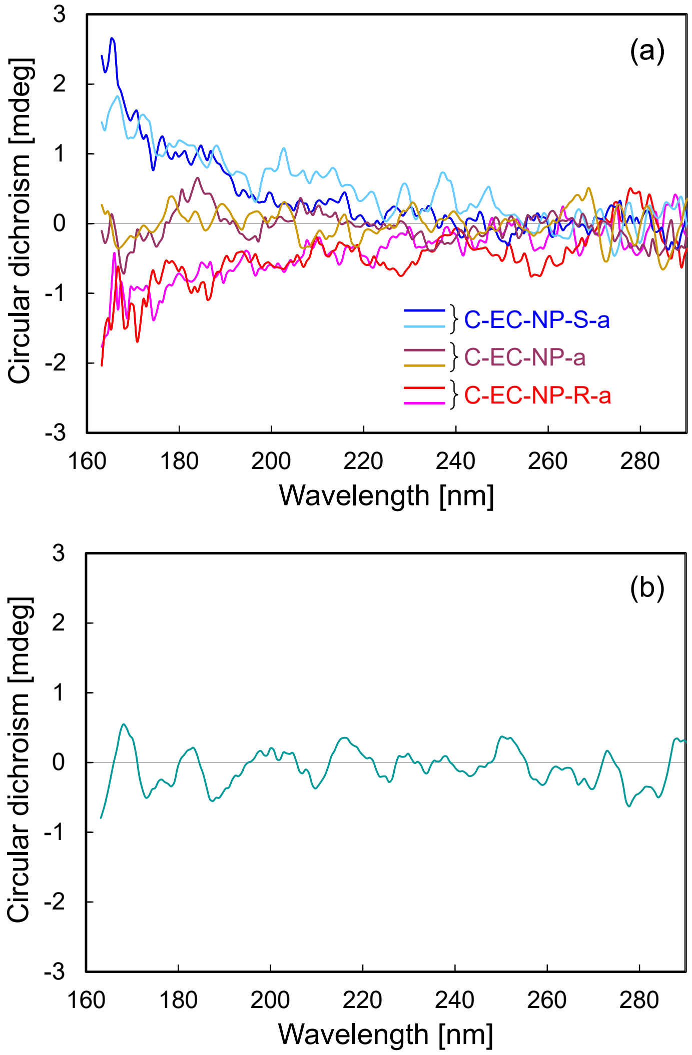

Figure S4. CD spectra for the three samples of C-EC-NP-S-a, C-EC-NP-R-a, and C-EC-NP-a, independently synthesized in the same method to confirm reproducibility (a) and reference CD spectrum for supernatant obtained by removing C-EC-NP-S-a from its dispersion to exclude the possibility of containing any eluted chiral molecule that could cause the CD signal (b).

XPS Spectra of Helically Aligned Fused CHNSs on MWCNTs

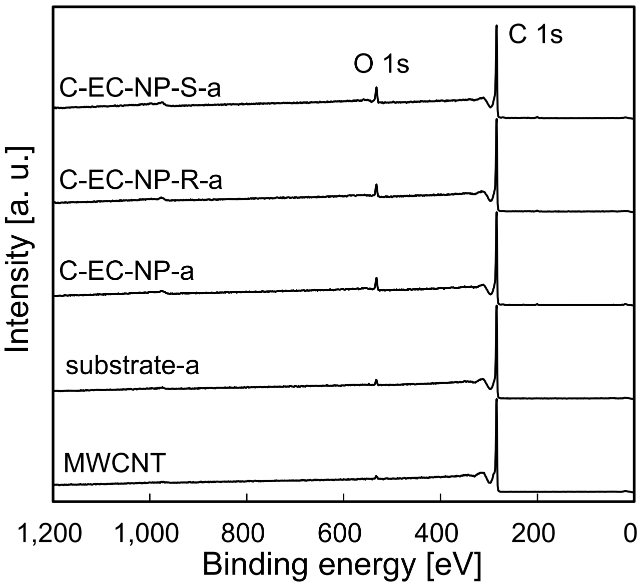

Figure S5. Wide-scan XPS spectra of MWCNTs, substrate-a, C-EC-NP-a, C-EC-NP-R-a, and C-EC-NP-S-a.

Raman Spectra of Amorphous Carbons Formed Without MWCNTs

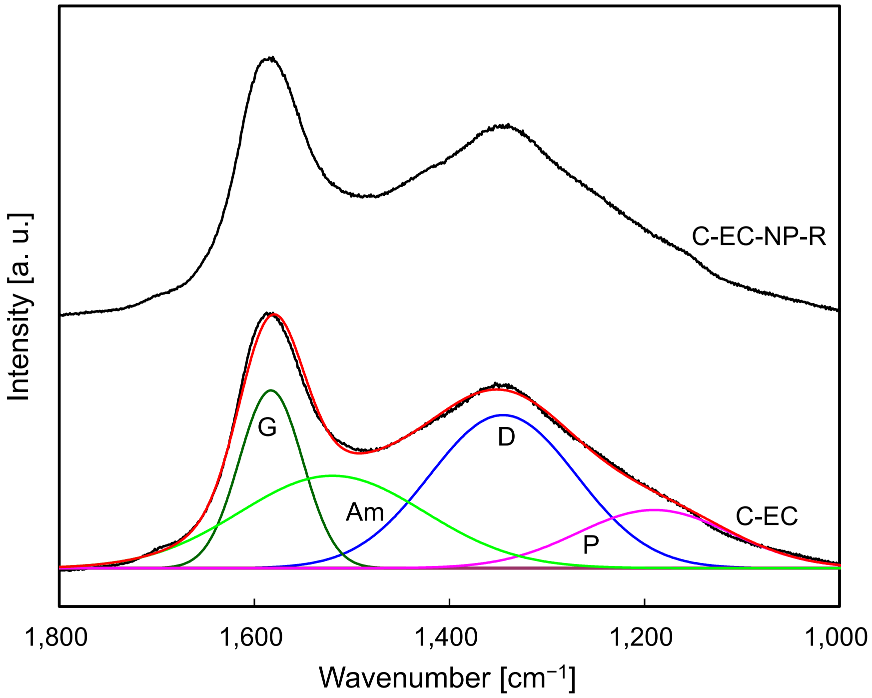

Figure S6. Raman spectra of carbonized ethyl cellulose (C-EC) and C-EC-NP-R formed without the MWCNT substrate. EC powder was carbonized at 550 °C for 1 h in an Ar atmosphere to synthesize C-EC. C-EC-NP-R without the MWCNTs was synthesized by dropping 0.1 cm^3 of the starting mixture used for EC-NP-R on a ⌀2 cm silica glass plate, evaporating the solvent at 30 °C, drying under vacuum at 90 °C, and carbonizing at 550 °C for 1 h in an Ar atmosphere.

Effect of Carbonization on Optical Activity

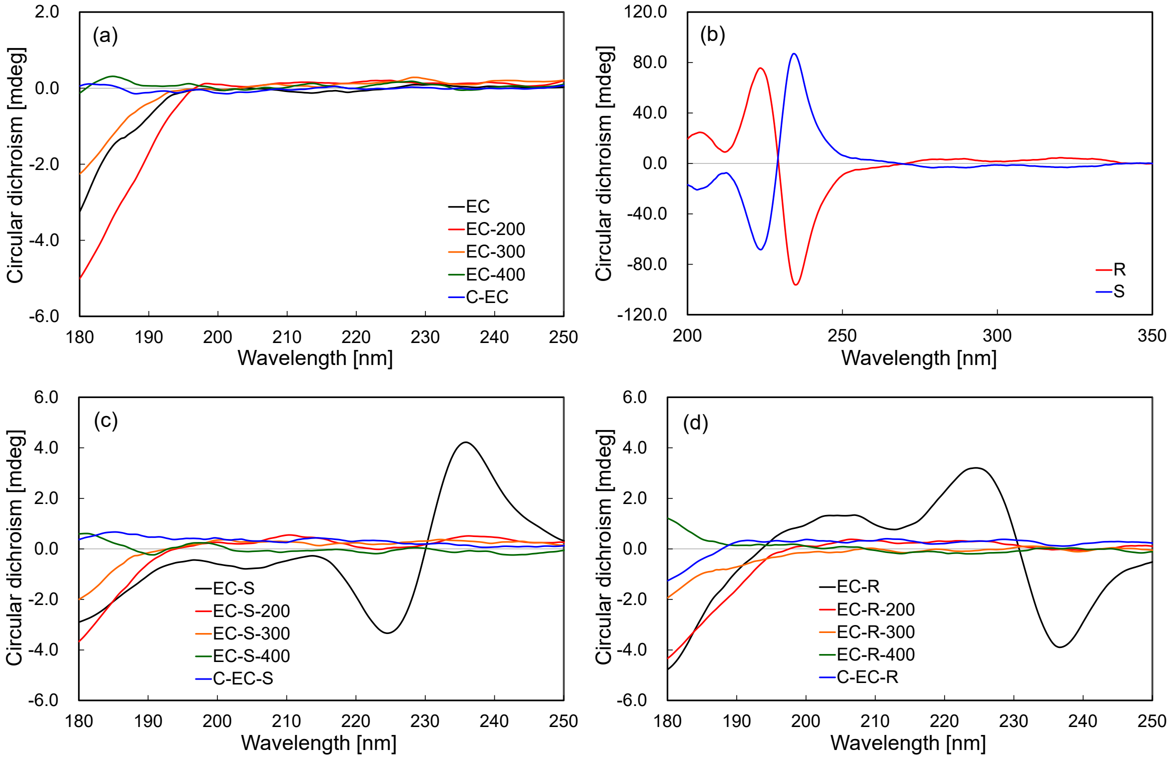

Figure S7. CD spectra of EC and heat-treated EC (a), (*R*)- and (*S*)-2,2′-bis(methoxymethoxy)-1,1′-binaphthyl (R and S, respectively) (b), EC-S and corresponding heat-treated samples (c), and EC-R and corresponding heat-treated samples (d). The temperatures used to prepare carbonization intermediates were 200, 300, and 400 °C. The carbonized samples (C-EC, C-EC-R, and C-EC-S) were synthesized at 550 °C.

TEM Images of Fe_3O_4 NP Alignment

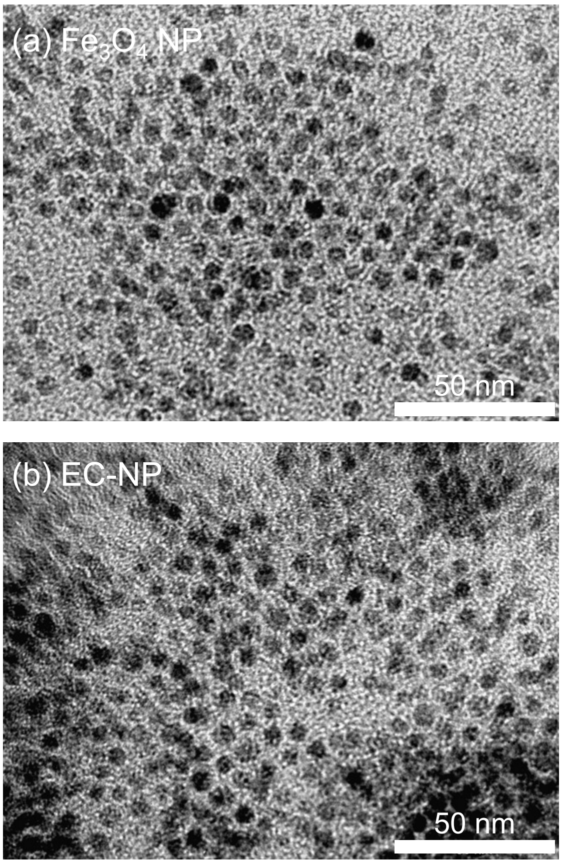

Figure S8. TEM images of Fe_3O_4 NPs fixed on grids from the Fe_3O_4 NP dispersion in toluene (a) and its mixture with EC (b).

FESEM Images of Precursors

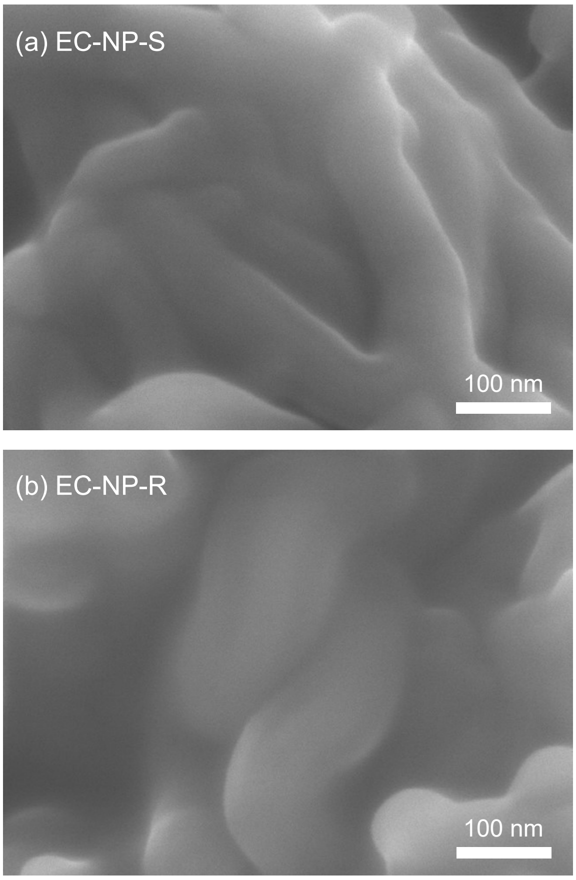

Figure S9. FESEM images of EC-NP-S (a) and EC-NP-R (b).

Decomposition of EC

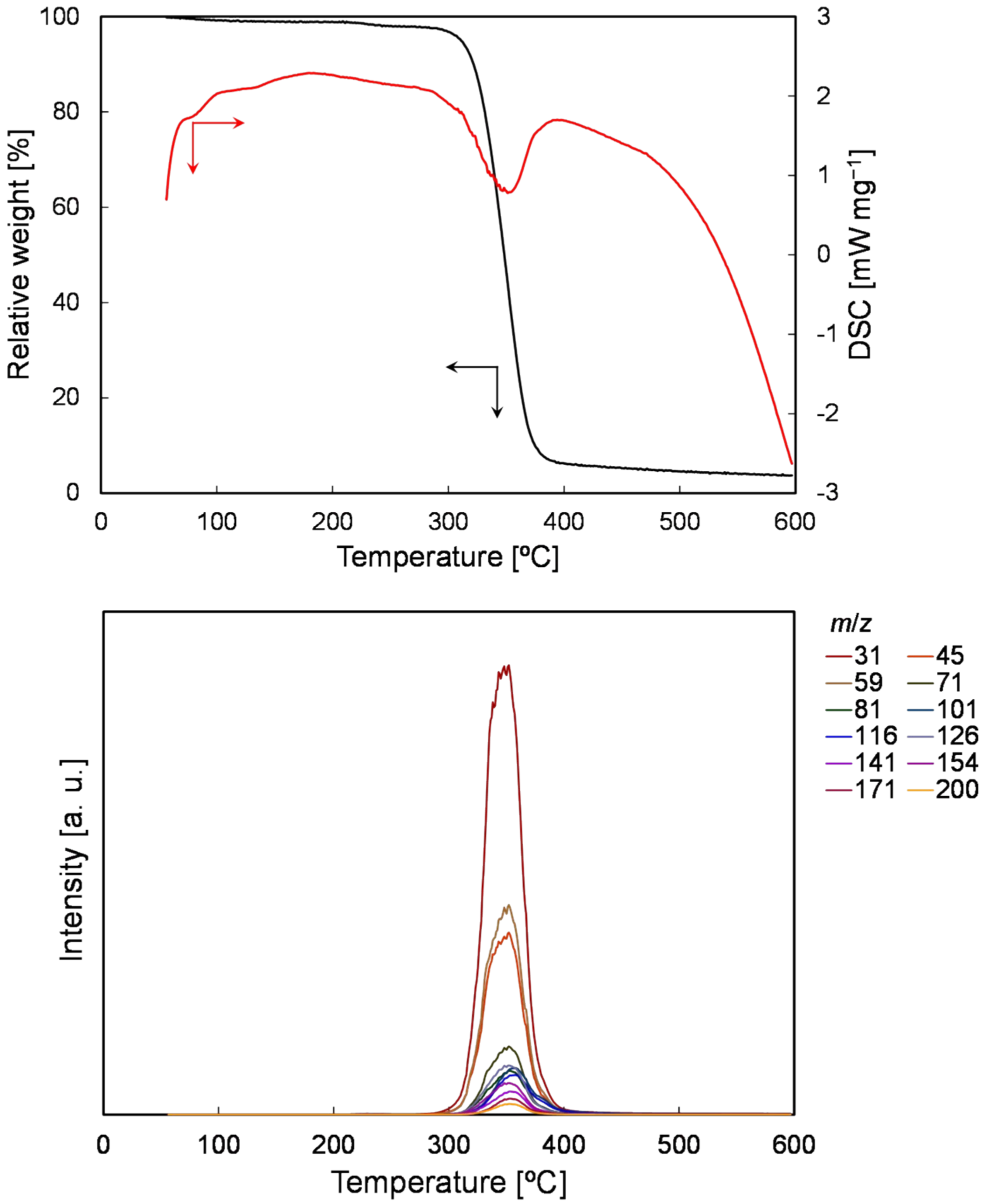

Figure S10. TG-DSC-MS profiles of EC.

Decomposition of Fe_3O_4 NPs

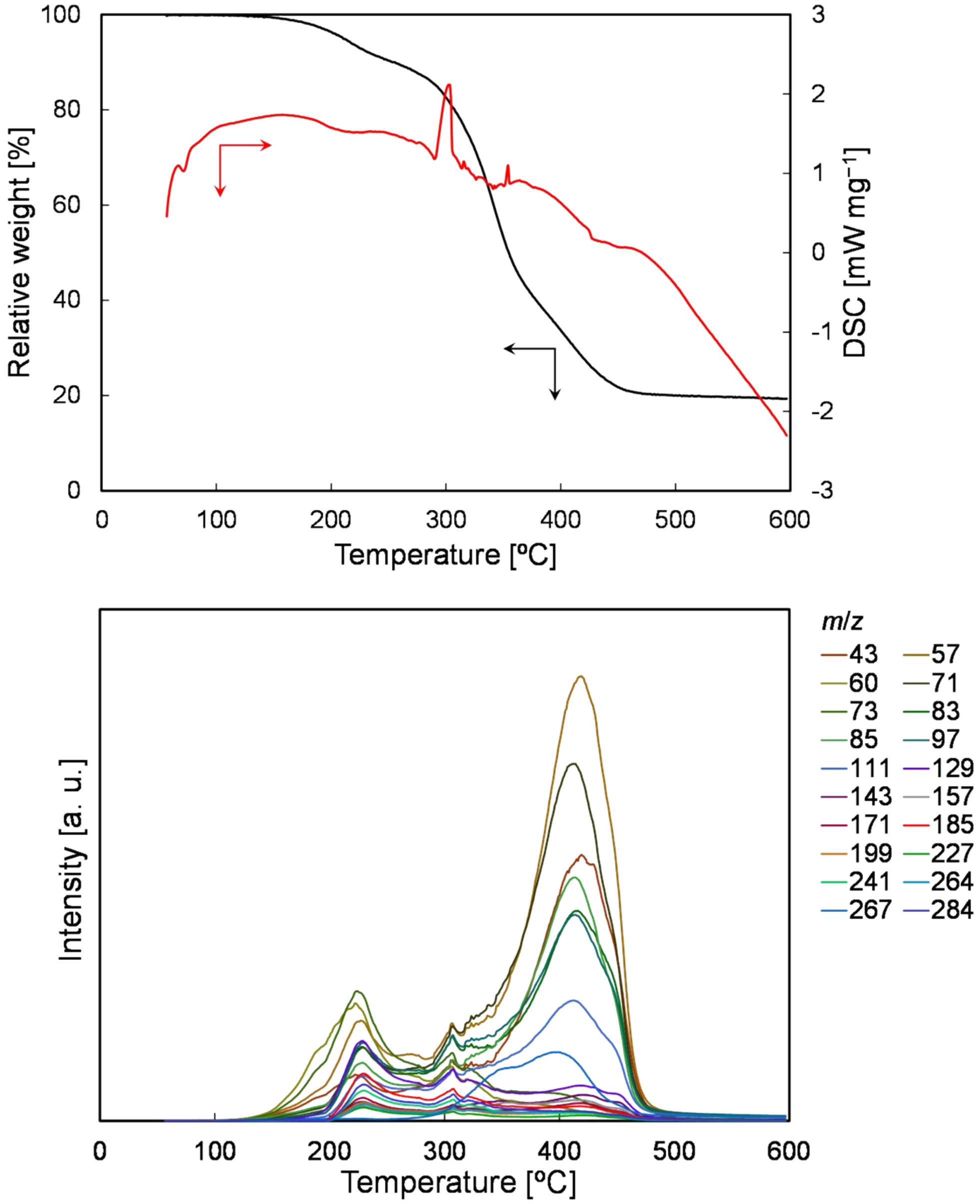

Figure S11. TG-DSC-MS profiles of Fe_3O_4 NPs with dispersant.

Decomposition of (*R*)-Binaphthyl Derivative

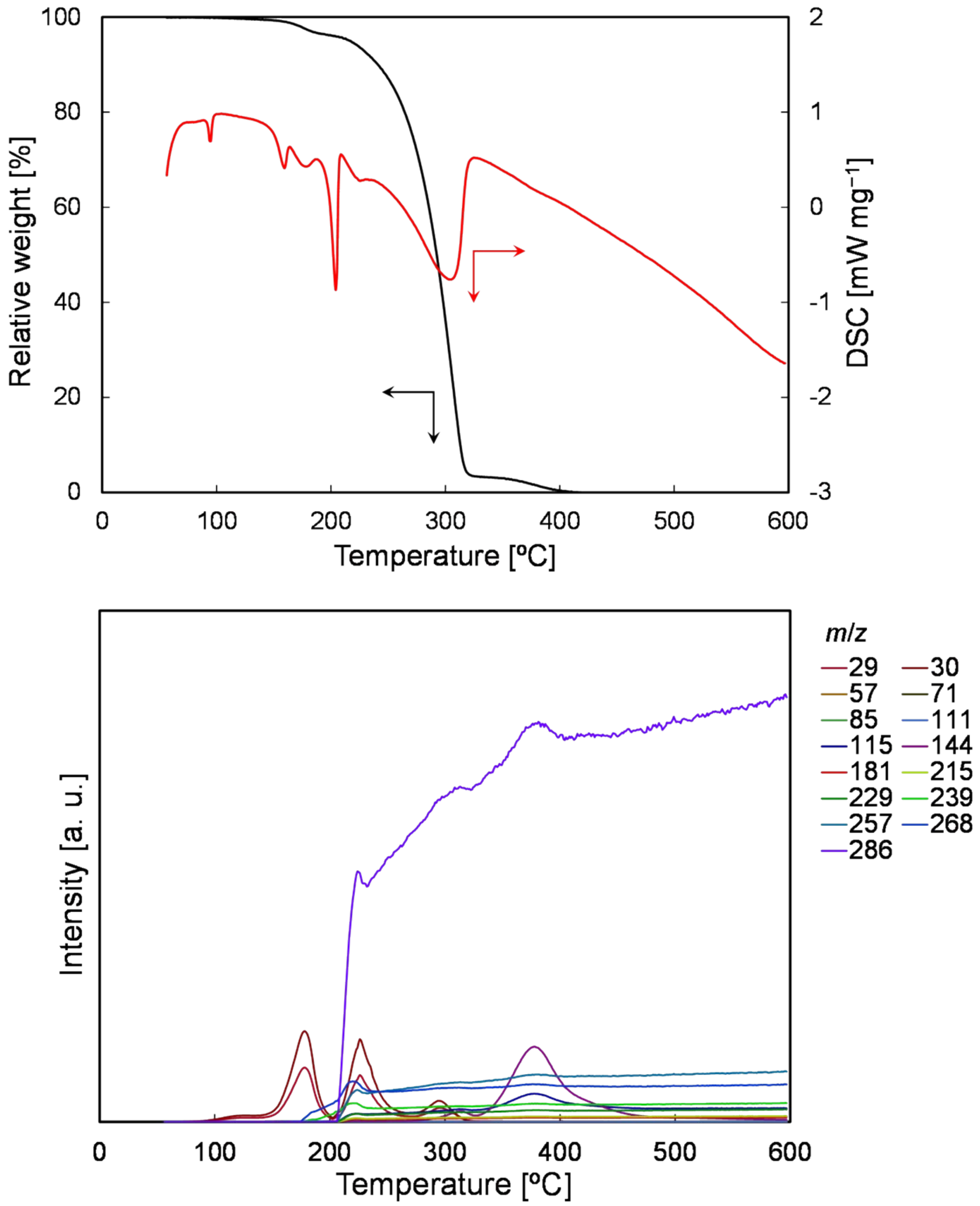

Figure S12. TG-DSC-MS profiles of (*R*)-2,2′-bis(methoxymethoxy)-1,1′-binaphthyl (purity, 99.1%, according to the manufacturer’s datasheet). The slight difference in the decomposition behavior of the (*R*)- and (*S*)-forms (shown in Figure S13) was attributed to impurities in the (*R*)-form.

Decomposition of (*S*)-Binaphthyl Derivative

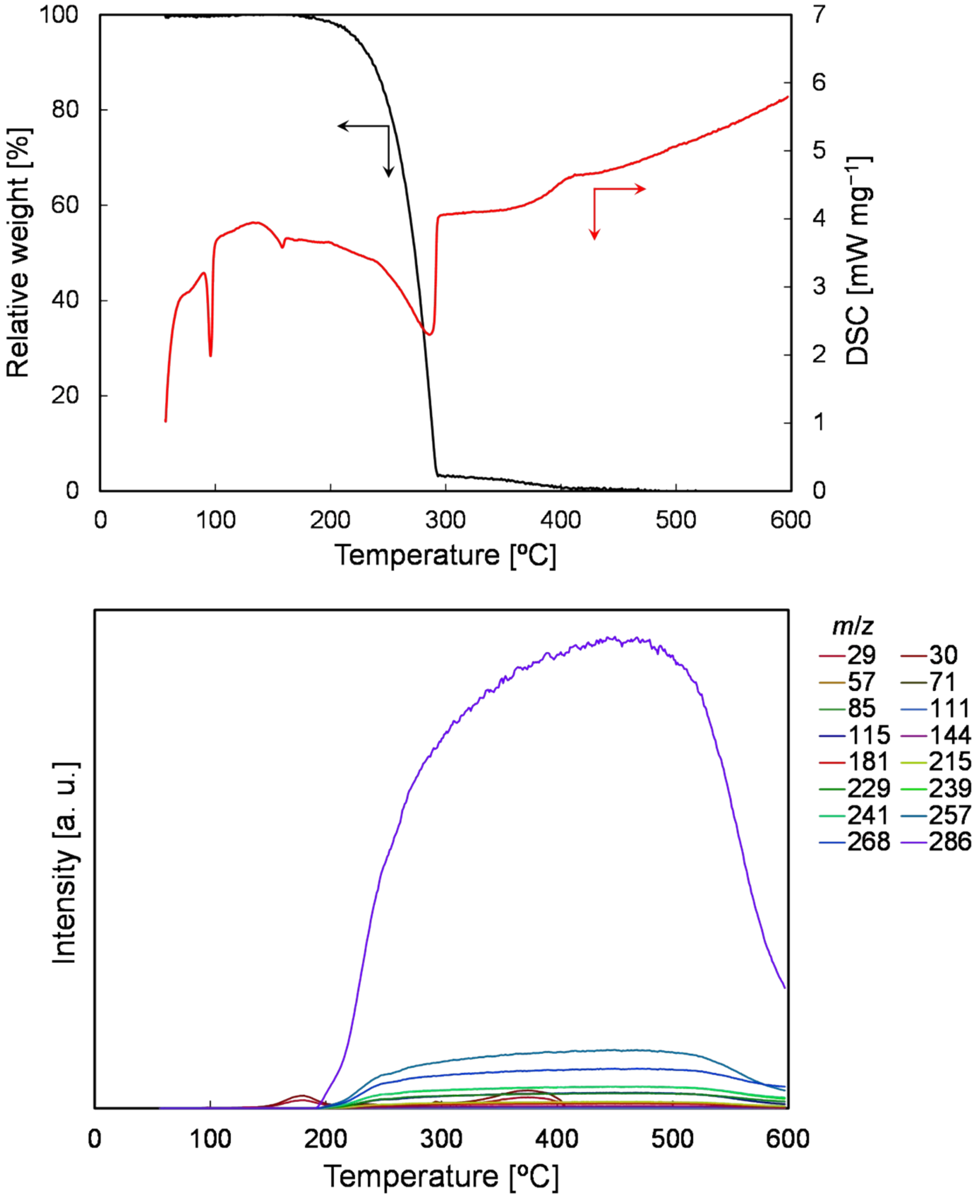

Figure S13. TG-DSC-MS profiles of (*S*)-2,2′-bis(methoxymethoxy)-1,1′-binaphthyl (purity, 100%, according to the manufacturer's datasheet).

Decomposition of Fe_3O_4 NPs with EC

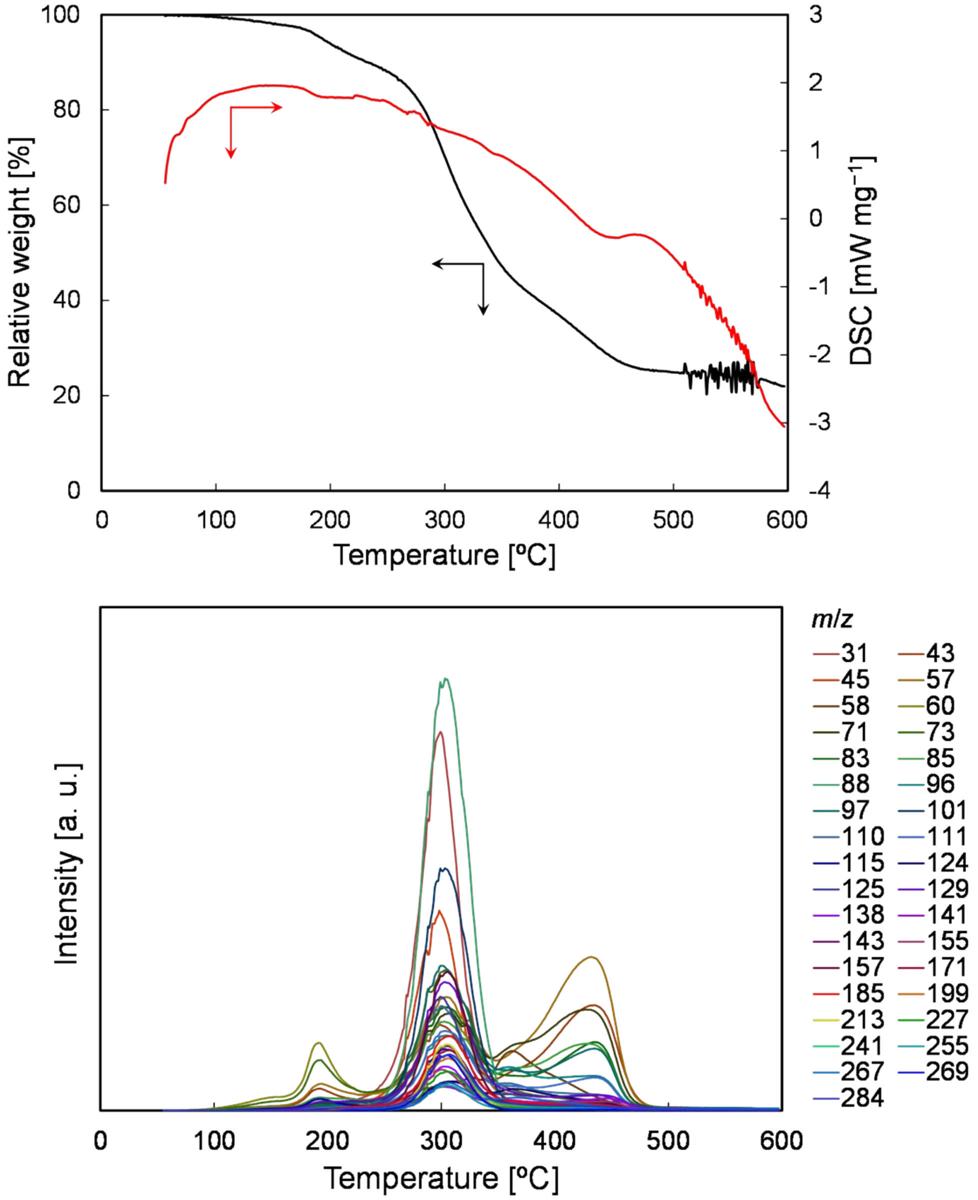

Figure S14. TG-DSC-MS profiles of a mixture of EC and Fe_3O_4 NPs with dispersant.

Decomposition of EC with (*R*)-Binaphthyl Derivative

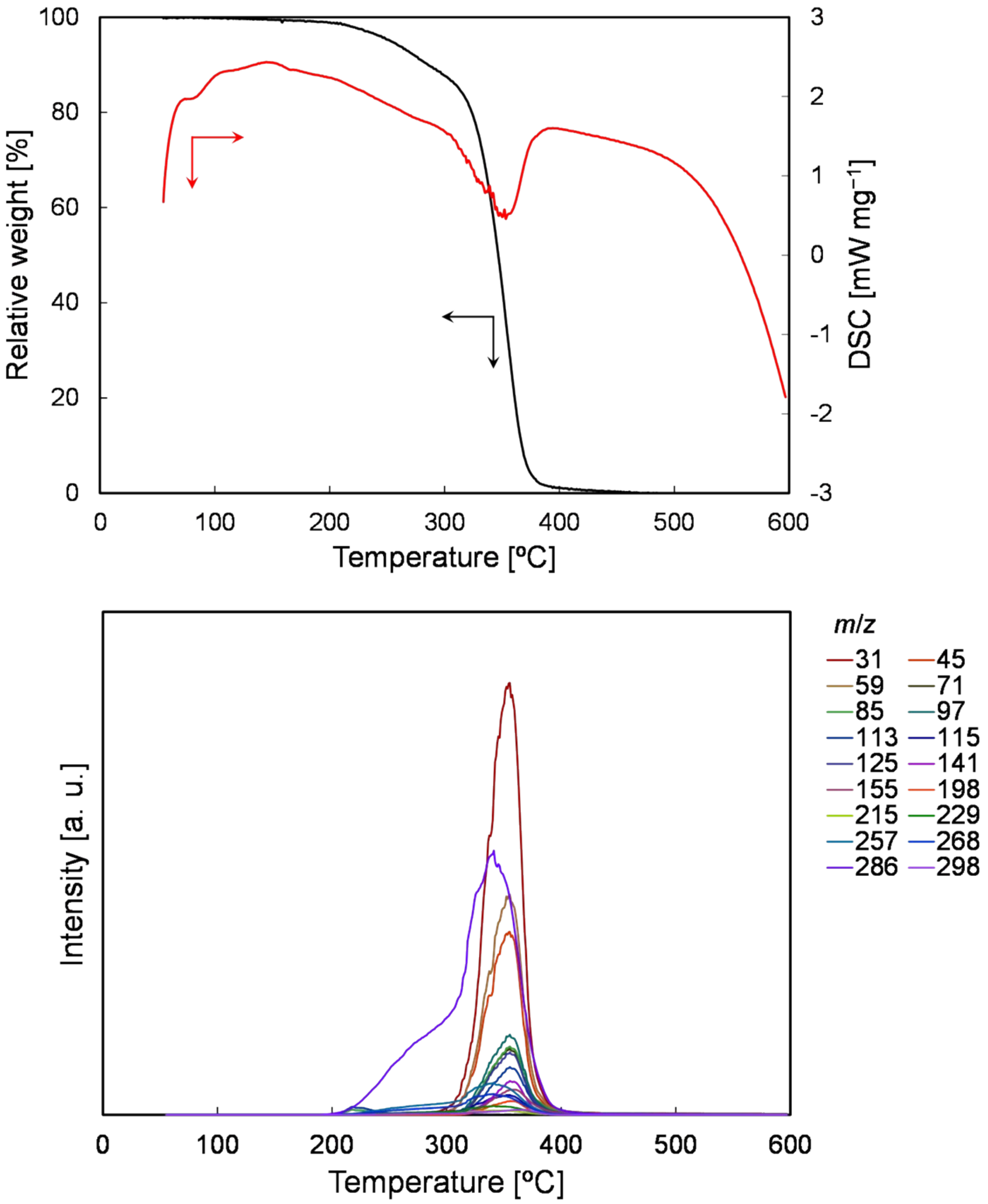

Figure S15. TG-DSC-MS profiles of a mixture of EC and (*R*)-2,2′-bis(methoxymethoxy)-1,1′-binaphthyl.

Decomposition of EC with (*S*)-Binaphthyl Derivative

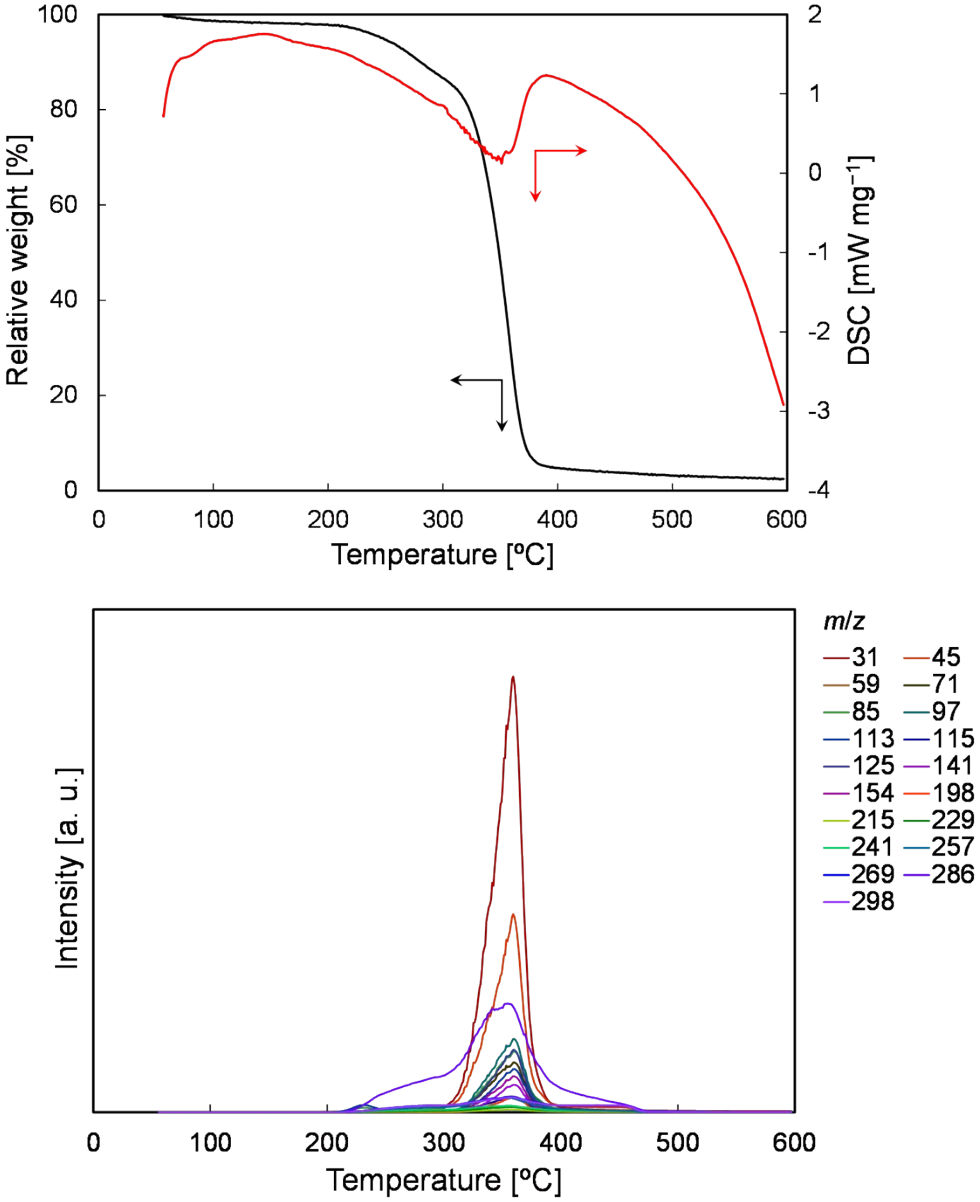

Figure S16. TG-DSC-MS profiles of a mixture of EC and (*S*)-2,2′-bis(methoxymethoxy)-1,1′-binaphthyl.

Decomposition of Fe_3O_4 NPs with EC and (*R*)-Binaphthyl Derivative

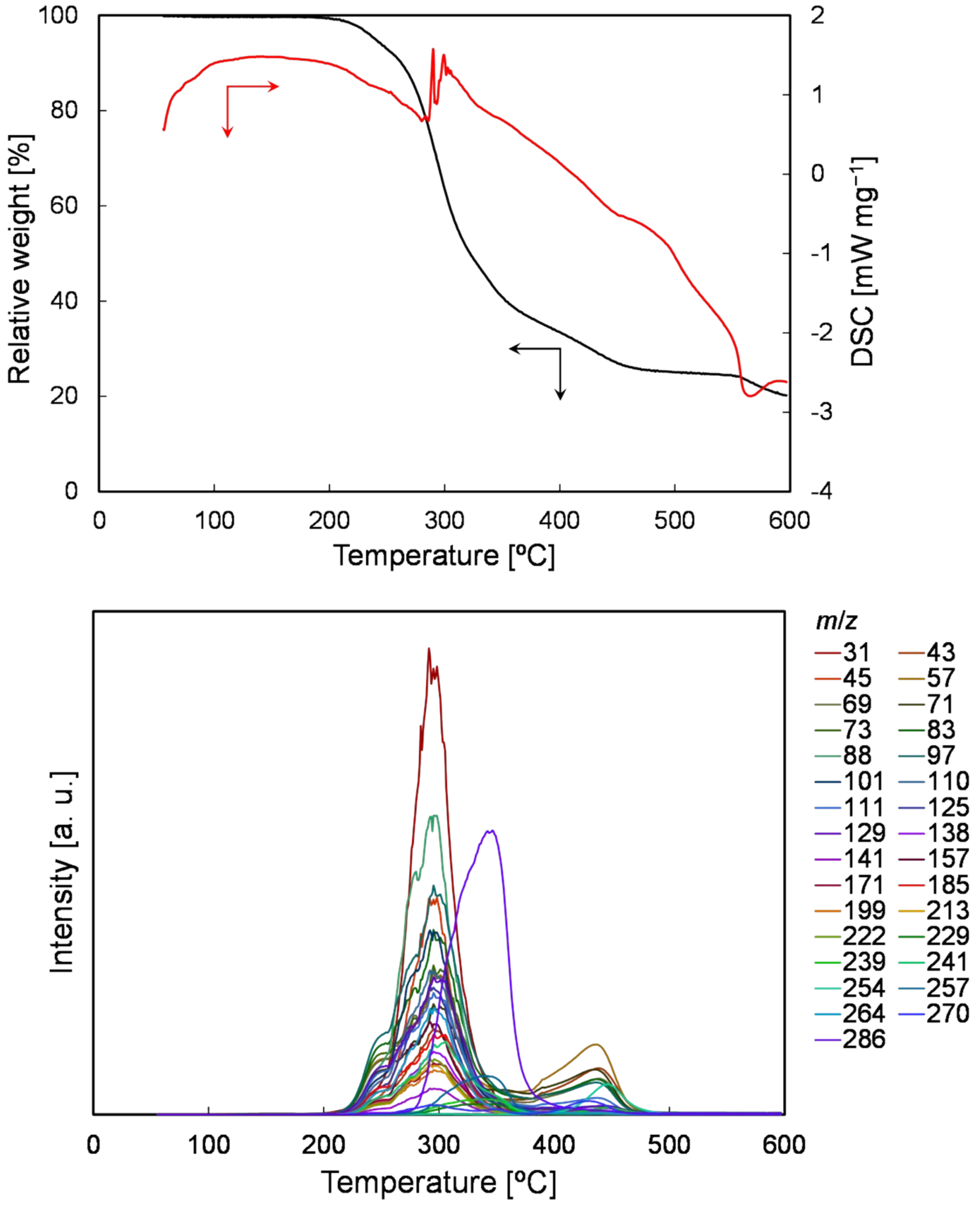

Figure S17. TG-DSC-MS profiles of a mixture of EC, Fe_3O_4 NPs with dispersant, and (*R*)-2,2′-bis(methoxymethoxy)-1,1′-binaphthyl.

Decomposition of Fe_3O_4 NPs with EC and (*S*)-Binaphthyl Derivative

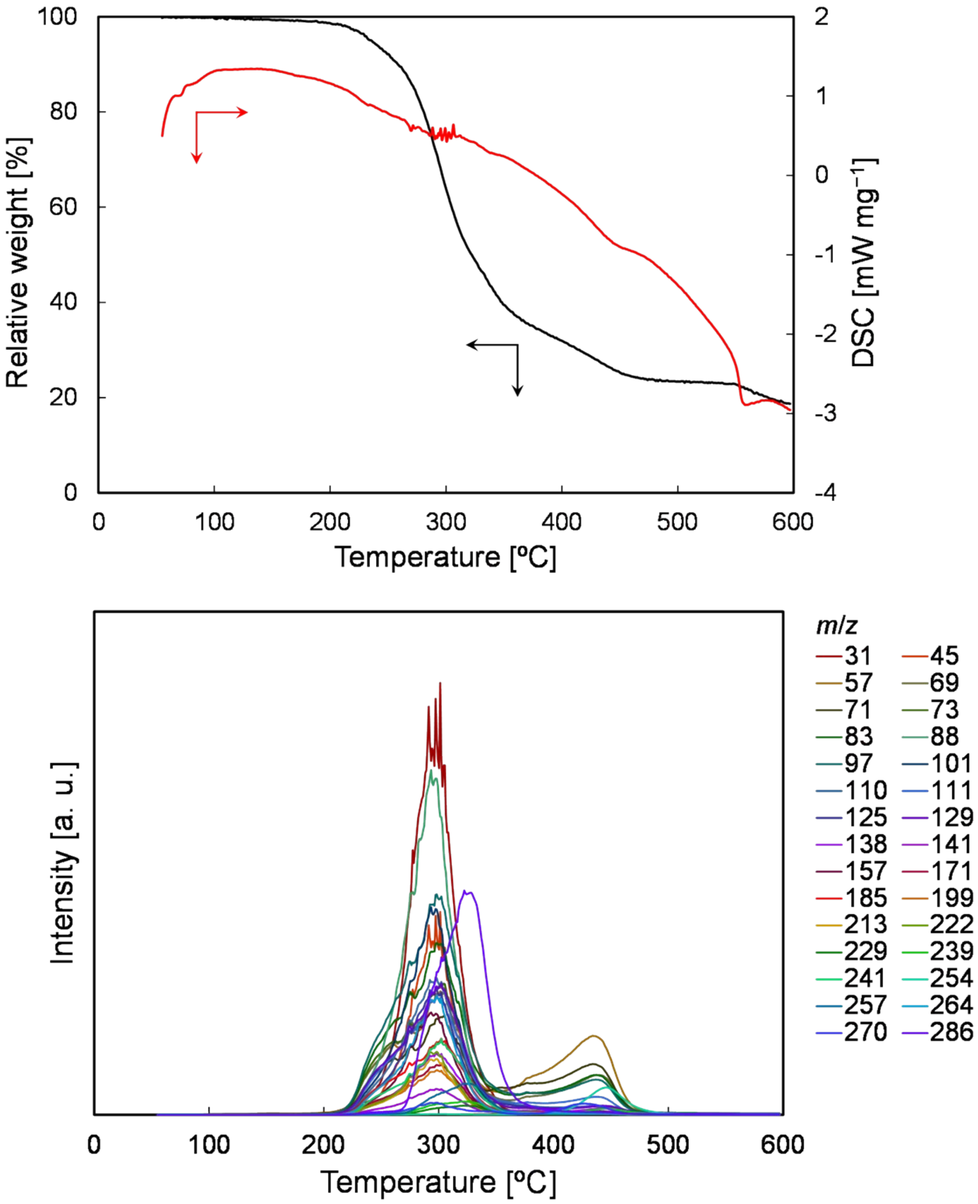

Figure S18. TG-DSC-MS profiles of a mixture of EC, Fe_3O_4 NPs with dispersant, and (*S*)-2,2′-bis(methoxymethoxy)-1,1′-binaphthyl.

Cyclic Voltammograms of Helically Aligned Fused CHNSs on MWCNTs

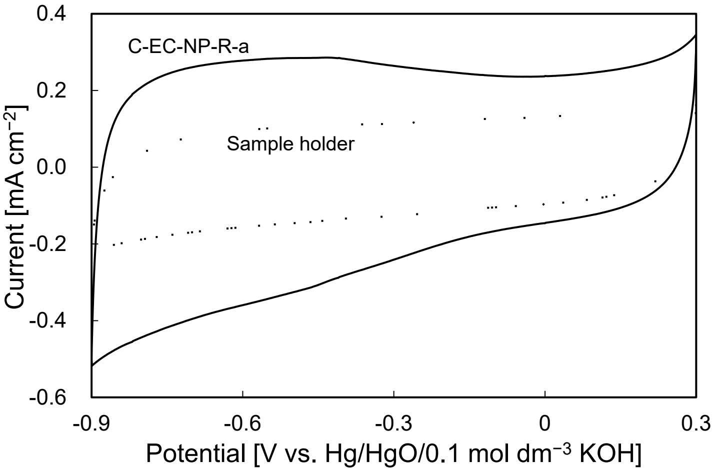

Figure S19. Cyclic voltammograms of sample holder (⌀8 mm, dotted line) and C-EC-NP-R-a (0.25 mg, solid line) electrode in Ar-saturated 0.1 mol dm^{-3} KOH aqueous solution at 25 °C (sweep rate: 10 mV s^{-1}).]

Effect of Carbon Surface Properties on Electrochemical Oxidation of BINOL

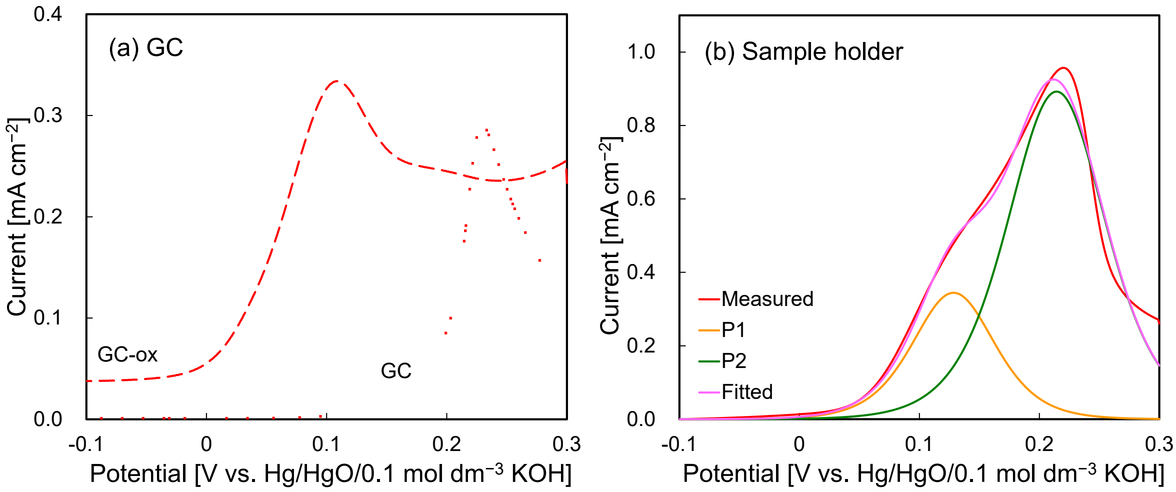

Figure S20. Linear sweep voltammograms of GC and GC-ox (a) and the sample holder (b) in 1 mmol dm^{-3} (*R*)-BINOL dissolved in Ar-saturated 0.1 mol dm^{-3} KOH aqueous solution at 25 °C (sweep rate: 10 mV s^{-1}). The peak deconvolution was based on the theoretical current–potential relationship for thin layer electrodes expressed by the following equation, wherein i is the current (A), n is the number of electrons, F is the Faraday constant (C mol^{-1}), v is the sweep rate (V s^{-1}), V is the volume of the thin layer (m^3), C is the bulk concentration of the reactant (mol m^{-3}), R is the gas constant (J mol^{-1} K^{-1}), T is the temperature (K), E is the potential (V), and $E^{0\prime}$ is the formal potential (V).[S1]

$$i = \frac{n^2F^2vVC}{RT}\,\frac{\exp\left[\left(\frac{nF}{RT}\right)\left(E - E^{0'}\right)\right]}{\left\{1 + \exp\left[\left(\frac{nF}{RT}\right)\left(E - E^{0'}\right)\right]\right\}^2}$$

The number of electrons calculated from the peak width was nearly 1, indicating that the following electrochemical reaction occurred.[S2]

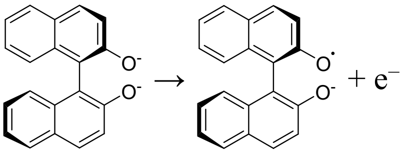

Electrochemical Oxidation of BINOL on Helically Aligned Fused CHNSs on MWCNTs

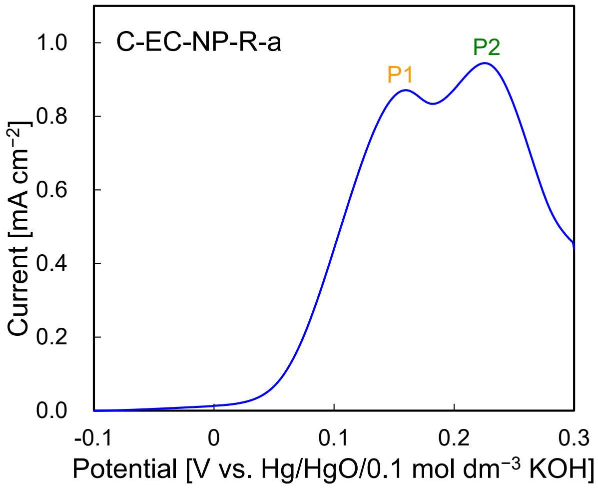

Figure S21. Linear sweep voltammogram of the C-EC-NP-R-a electrode in 1 mmol dm^{-3} (*S*)-BINOL dissolved in Ar-saturated 0.1 mol dm^{-3} KOH aqueous solution at 25 °C (sweep rate: 10 mV s^{-1}).

Cyclic Voltammograms after BINOL Electrochemical Oxidation Measurements

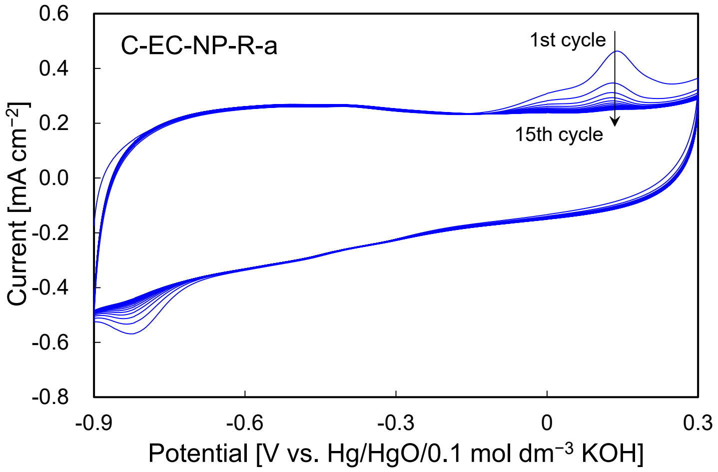

Figure S22. Cyclic voltammograms of the C-EC-NP-R-a electrode in Ar-saturated 0.1 mol dm^{-3} KOH aqueous solution at 25 °C (sweep rate: 10 mV s^{-1}) after measurement of the linear sweep voltammogram in 1 mmol dm^{-3} (*S*)-BINOL dissolved in Ar-saturated 0.1 mol dm^{-3} KOH aqueous solution. The shoulder peak at 0.0 V is attributed to the oxidation of reduced species generated during the negative scan from 0.3 to −0.9 V before recording the repeated scans. The electrode surface was almost recovered after the 15th potential cycle.

Peak Deconvolution of Linear Sweep Voltammogram for BINOL Electrochemical Oxidation

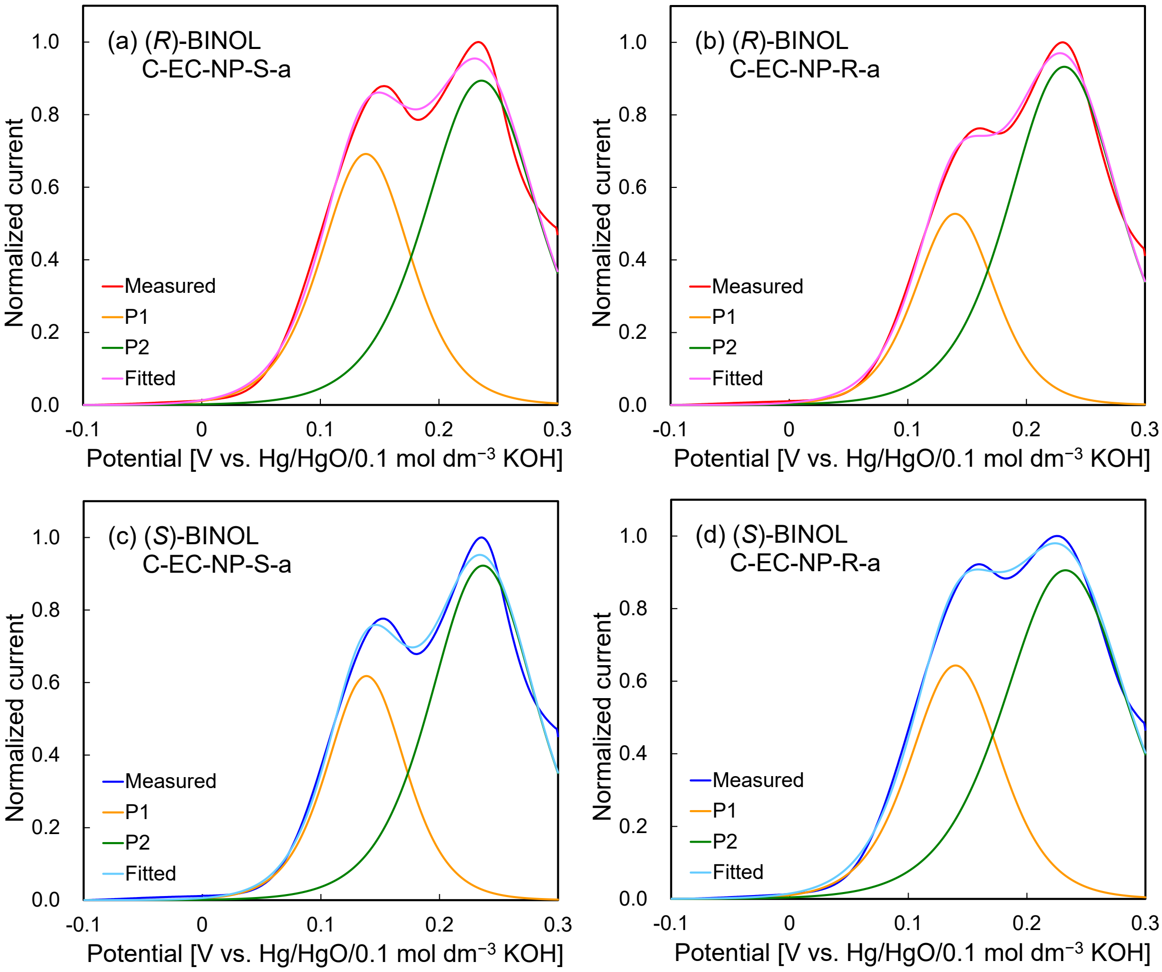

Figure S23. Linear sweep voltammograms of C-EC-NP-S-a (a,c) and C-EC-NP-R-a (b,d) electrodes in 1 mmol dm^{-3} (*R*)-BINOL (a,b) or (*S*)-BINOL (c,d) dissolved in Ar-saturated 0.1 mol dm^{-3} KOH aqueous solution at 25 °C (sweep rate: 10 mV s^{-1}).

Electrochemical Oxidation of FcA on Helically Aligned Fused CHNSs on MWCNTs

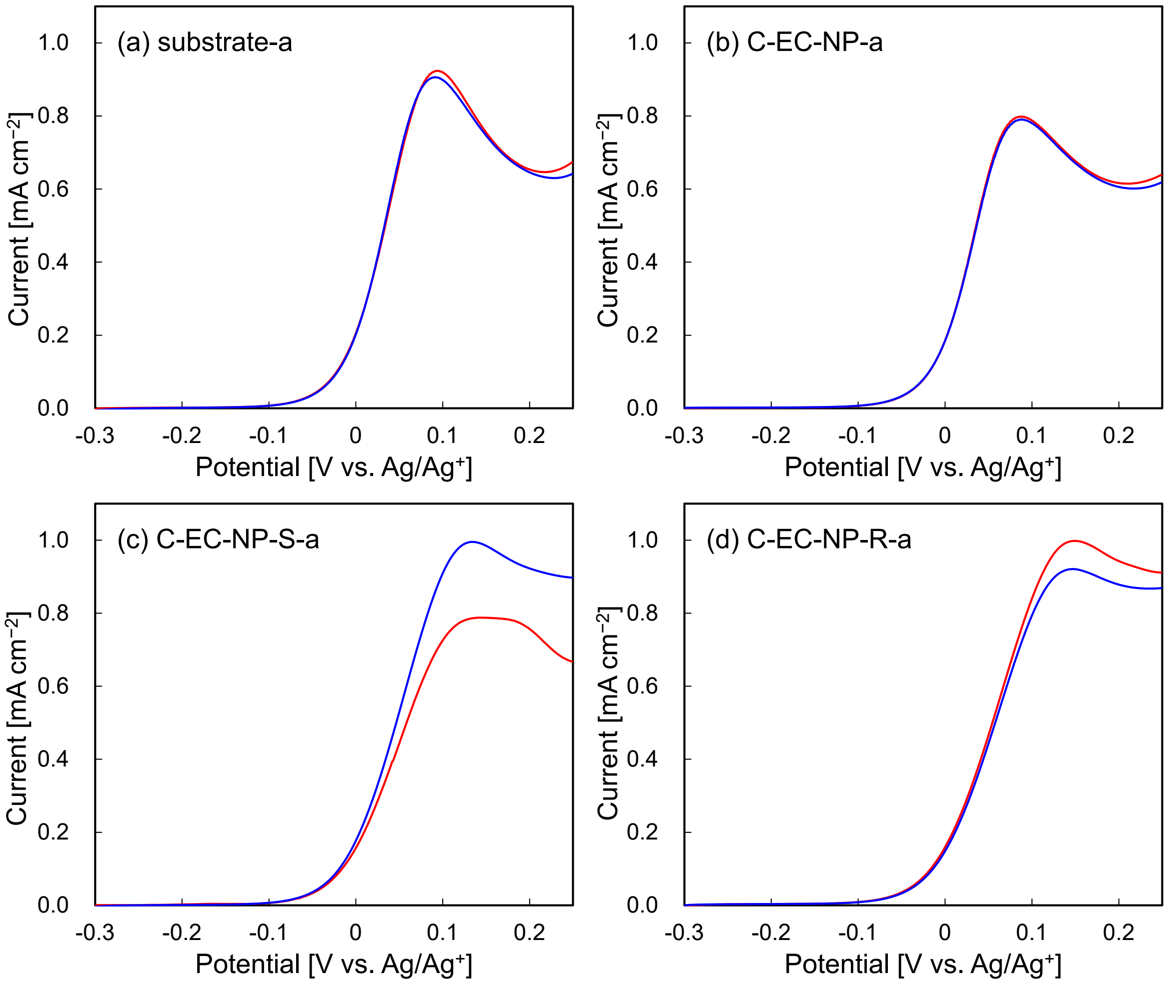

Figure S24. Helically aligned fused CHNSs used as chiral electrodes in a nonaqueous system. Linear sweep voltammograms of substrate-a (a), C-EC-NP-a (b), C-EC-NP-S-a (c), and C-EC-NP-R-a (d) in 10 mmol dm^{-3} (*R*)-(+)- (—) and (*S*)-(−)-FcA (—) dissolved in Ar-saturated 0.1 mol dm^{-3} $LiClO_4$ acetonitrile solution at 25 °C (sweep rate: 10 mV s^{-1}).

Cyclic Voltammograms after FcA Electrochemical Oxidation Measurements

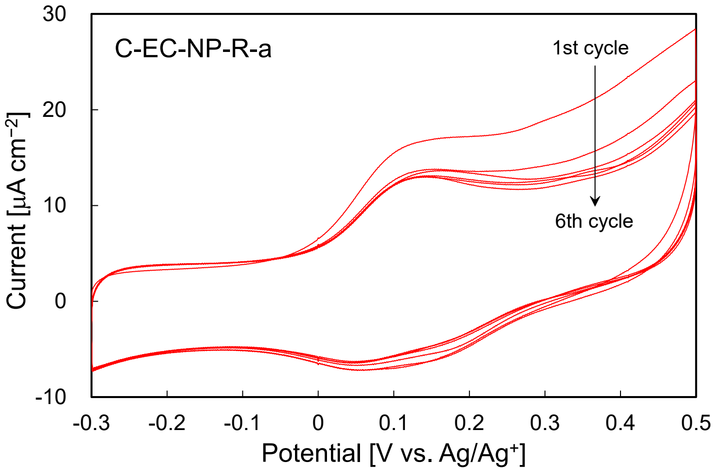

Figure S25. Cyclic voltammograms of C-EC-NP-R-a in Ar-saturated 0.1 mol dm^{-3} $LiClO_4$ acetonitrile solution at 25 °C (sweep rate: 10 mV s^{-1}) after measurement of the linear sweep voltammogram in 1 mmol dm^{-3} (*R*)-(+)-FcA dissolved in Ar-saturated 0.1 mol dm^{-3} $LiClO_4$ acetonitrile solution. Nearly stable voltammograms were observed after the 6th cycle with residual Fe redox peaks, which were sufficiently small compared to the FcA oxidation peak observed in the 1 mmol dm^{-3} FcA solution (Figure S24) and thus had almost negligible influence on the chiral discrimination.

Spatial Arrangements of Helically Aligned Fused CHNSs on MWCNTs and Chiral Guests

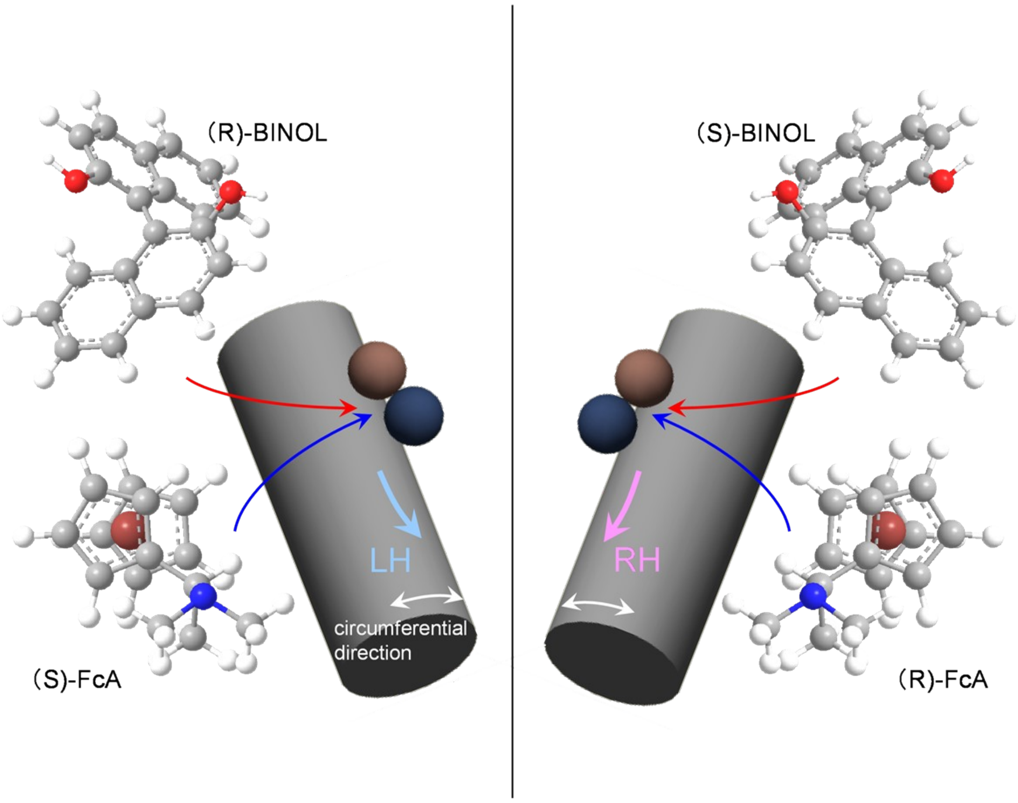

Figure S26. Summary of relationships between helical alignments and chiral guests that fit into the chiral spaces resulting from the helical alignments. The fitting of the guest molecules into the chiral space can be explained by hypothesizing that the long axis of each guest molecule, i.e., naphthalene–naphthalene in BINOL and cyclopentadienyl–Fe–cyclopentadienyl in FcA,[S3] lies along the circumferential direction of the MWCNTs.

References

[S1] A. J. Bard and L. R. Faulkner, in *Electrochemical methods: Fundamentals and applications, 2nd Edition*, John Wiley & Sons, New York, 2001.

[S2] Q. Lin, Q. Li, C. Batchelor-McAuley and R. G. Compton, *J. Phys. Chem. C*, 2015, **119**, 1489.

[S3] P. J. Hubbard, J. W. Benzie, V. I. Bakhmutov and J. Blümel, *Organometallics*, 2020, **39**, 1080.